Title

Characterizing regional-scale temporal evolution of air dose rates after the Fukushima Daiichi Nuclear Power Plant accident

Authors

Wainwright, Haruko M

Seki, Akiyuki

Mikami, Satoshi

et al.

Publication Date

2018-09-01

DOI

10.1016/j.jenvrad.2018.04.006

Peer reviewed

Characterizing regional-scale temporal evolution of air dose rates after the Fukushima Daiichi Nuclear Power Plant accident

Haruko M. Wainwright[a] Akiyuki Seki[b] Satoshi Mikami[c] KimiakiSaito[d]

Abstract

In this study, we quantify the temporal changes of air dose rates in the regional scale around the Fukushima Dai-ichi Nuclear Power Plant in Japan, and predict the spatial distribution of air dose rates in the future. We first apply the Bayesian geostatistical method developed by Wainwright et al. (2017) to integrate multiscale datasets including ground-based walk and car surveys, and airborne surveys, all of which have different scales, resolutions, spatialcoverage, and accuracy. This method is based on geostatistics to represent spatial heterogeneous structures, and also on Bayesian hierarchical models to integrate multiscale, multi-type datasets in a consistent manner. We apply this method to the datasets from three years: 2014 to 2016. The temporal changes among the three integrated maps enables us to characterize the spatiotemporal dynamics of radiation air dose rates. The data-driven ecological decay model is then coupled with the integrated map to predict future dose rates. Results show that the air dose rates are decreasing consistently across the region. While slower in the forested region, the decrease is particularly significant in the town area. The decontamination has contributed to significant reduction of air dose rates. By 2026, the air dose rates will continue to decrease, and the area above 3.8 μSv/h will be almost fully contained within the non-residential forested zone.

1. Introduction

Six years has passed since the radionuclide release occurred at the Fukushima Dai-ichi Nuclear Power Plant (FDNPP). During the accident, radionuclides were deposited on soil and plants through wet and dry deposition (Tanaka, 2012). Radiocesium (^{134}Cs and ^{137}Cs) is currently the main contaminant in the environment (Saito, 2016). Over the past six years, the region around FDNPP has experienced remarkable recovery. The current evacuation designated area has shrunk to 370 km^2 in April 2017, which is 2.7% of the Fukushima Prefecture (Fukushima Prefectural Government, 2017). The extensive decontamination effort has played a critical role in this recovery process (Yasutaka et al., 2013). In addition, many studies have

reported that the decrease in the air dose rates – including the reductionassociated with radiocesium transport in the environment – has been accelerated compared to the physical decay (Kinase et al., 2014, Kinase et al., 2017). It has been found that the air dose rates have reduced to around one fourth in the undisturbed flat land and one fifth on the urban roads in the first four years (Saito, 2016).

An extensive monitoring program has been established after the accident and still continues to this day (Mikami et al., 2015a; Saito and Onda, 2015). One of the main goals in the monitoring program has been to map radiation dose rates, i.e., the ambient dose equivalentrates, in a regional scale based on the datasets collected by different agencies (Saito, 2016). The datasets have been carefully archived and made accessible to the public (Seki et al., 2014). The monitoring program has been playing a central role towards ensuring the public safety and preparing for decontamination efforts and residents' return. In addition, monitoring has provided information critical to understand the transport behavior of radiocesium in the environment (Saito, 2016).

There are a variety of monitoring platforms and data available in the regions. In addition to continuous-time monitoring posts, spatially extensive datasets include airborne, car and walk surveys once or twice a year. Car surveys are based on a GPS-aided mobile radiation monitoring system, the Kyoto University Radiation Mapping system (KURAMA), which has been used extensively to characterize the distribution of air dose rates along the roads in real time (Andoh et al., 2015; Tanigaki et al., 2013). In walk surveys, people carry around the same KURAMA-II systems in small streets and various places outside where people walk around, so that the potential external dose outside can be mapped in detail. Airborne surveys have provided vital information to map the air dose rates across the region (Torii et al., 2012). These measurements of air dose rates have been also considered an excellent proxy for radiocesium contamination in soil at flat fields (Mikami et al., 2015b; Saito et al., 2015).

Changes in air dose rates have been characterized extensively based on these monitoring datasets, aiming to describe and predict the reduction of radiation air dose rates in the environment (Kinase et al., 2014, Kinase et al., 2015). Although there have been efforts to model radionuclide transport mechanistically in the near surface environment (e.g., Kitamura et al.,

2014; Wei et al., 2017), the exact prediction has been challenging, since the transport involves numerous spatially and temporally heterogeneous factors difficult to measure over time and space. In particular, the radiocesium transport in urban areas is known to be dictated by anthropologic impacts such as traffic and human movements (Andoh et al., 2015). Such enhanced reduction in air dose rates can be defined as environmental or ecological decay, and described by data-driven models with the environmental or ecological half-life (Peles et al., 2002). In the Fukushima region, a significant effort was made to develop data-driven models and to compute the rate of ecological decay (e.g., Kinase et al., 2014, Kinase et al., 2017).
However, it has been difficult to quantify the heterogeneity of environmental decay in the regional scale, since spatially extensive airborne survey datasets often have discrepancy with the ground-based measurements and have a larger uncertainty due to the large measurement footprints, and atmospheric effects. In addition, the complex terrain in the forested mountainous region is considered to increase uncertainty (Torii et al., 2012).
Recently, Wainwright et al. (2017) developed a Bayesian hierarchical modeling approach to integrate multiscale datasets (i.e., car, walk and airborne surveys), and also to estimate the spatial distribution of air dose rates in high resolution over space. They estimated the air dose rates equivalent to walk surveys, since walk surveys represent the exposure of an average person walking outside. The integrated air dose-rate maps are more accurate than the airborne data alone, having less bias and uncertainty.
In this study, our goals are (1) to quantify the temporal changes of air dose rates in the regional scale, (2) to identify the characteristics of environmental decay rates depending on land-use, and (3) to predict air dose rates in the future. We focus on the evacuation designated area and the region where the restriction order was recently lifted in March 2017. We first extend the approach by Wainwright et al. (2017) to a larger area covering this region, and create multiple integrated maps every year at the time when the airborne datasets were collected. Then we characterize the changes in air dose rates, including the effect of decontamination in villages and urban areas. Our results are expected to help inform efforts to plan for the residents' return and decontamination efforts in the area currently designated for evacuation.

2. Materials and methods

2.1. Site and data

The area of interest in this study includes the current evacuation designated area, and the area where the restriction order was recently lifted in March 2017 (Fig. 1a). It extends from the FDNPP location to the northwest, following the radioactive plume during the accident. This area –approximately 730 km^2 – is mostly forested with 16% of the land used for agriculture, 83% forested, and just 1% representing urban use, according to the high-resolution land-use and land-cover map of Japan (version 14.02) created by Japan Aerospace Exploration Agency (Takahashi et al., 2013). This area extends from the coast towards the mountains, with the altitude ranging from 0 m to about 1000 m above the sea level.

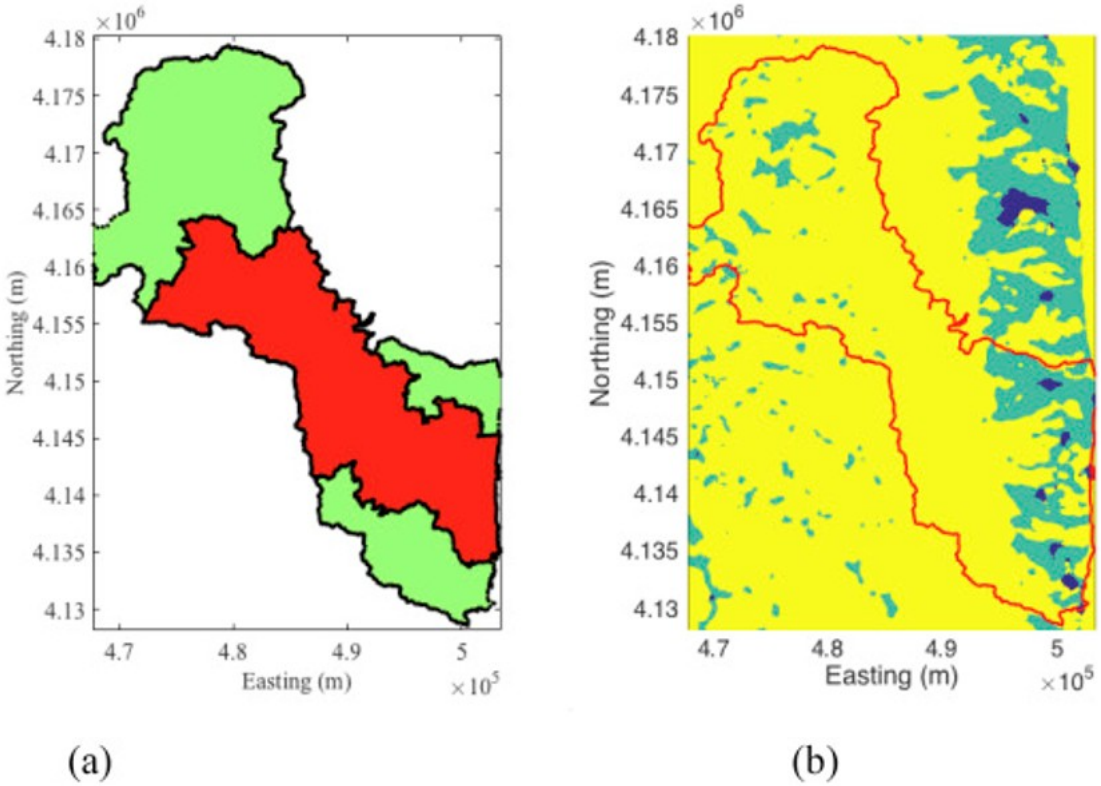

Fig. 1. (a) Evacuation designated area and (b) land cover types (blue = urban, green = cropland and yellow = forest). In (a), the red region is the evacuation designated area as of April 2017. The green region is where the restriction order was lifted in April 2017.

In the same manner as Wainwright et al. (2017), we used the three types of air dose rate datasets compiled by Japan Atomic Energy Agency (JAEA). The car survey datasets used in our study were acquired through the publically

available database (http://emdb.jaea.go.jp/emdb/en/) and collected using the KURAMA-II systems along the major roads. The KURAMA-II system included a CsI(Tl) scintillation detector, GPS and a software-designed control device (Tsuda et al., 2015). The calibration was done using gamma rays from radioisotope sources at the Facility of Radiation Standard and the Instrument Calibration Facility in JAEA. The dose rate was measured automatically along with the GPS location every 3 s, while the car was moving in the legal speed or along with the traffic. The datasets were averaged within the 100 m-by-100 m mesh. The walk survey datasets were provided by JAEA after averaging the data values within the 20 m-by-20 m mesh. The walk survey used the KURAMA-II system as well. In addition, we used the publically available air survey datasets that were calibrated to the equivalent dose rates to the one 1 m-above ground (Torii et al., 2012). The datasets were given within the 250 m-by-250 m mesh after interpolation using the IDW (inverse distance weighting) method.

Although the types of datasets are the same as those used in Wainwright et al. (2017), there are some differences. The dose rate is generally higher in the evacuation designated area than Fukushima City used for the estimation in the previous study. It is known that the air dose rate reduction tendencies are different in the evacuation zone due to the lack of human activities (Saito, 2016). In addition, the evacuation designated area has a larger spatial coverage of forested areas with less human activities. The spatial coverage of car and walk surveys is therefore limited compared to the spatial data coverage in Fukushima City.

2.2. Methodology

We use the data integration methodology developed by Wainwright et al. (2017). Although the detailed description is available in Wainwright et al. (2017), we briefly summarize the methodology here for completeness. Our data integration is based on a Bayesian hierarchical model, which consists of statistical sub-models: data models and process models (Wikle et al., 2001). The process models–in this context–describe the spatial pattern (or map) of air dose rates within the domain, representing the spatial trend and heterogeneity of contamination. We use a geostatistical model to describe this spatial pattern (Deutsch and Journel, 1998; Ribeiro and Diggle, 2007).

The goal is to estimate the air dose rates equivalent to walk surveys, since walk surveys represent the exposure of an average person walking outside. To develop an integrated map, we denote the radiation dose rate at i-th pixel by y_i, where $i = 1, \ldots, n$. We also denote three datasets by three vectors, representing the airborne surveydata $\boldsymbol{z}_A$ (each data point is represented by $\boldsymbol{z}_{A,j}$, where $j = 1, \ldots, m_A$), car survey data $\boldsymbol{z}_C$ (each data point is represented by $\boldsymbol{z}_{C,j}$, where $j = 1, \ldots, m_C$), and walk survey data (each data point is represented by $\boldsymbol{z}_{W,j}$, where $j = 1, \ldots, m_W$). The goal is to estimate the posterior distribution of the radiation dose-rate map $\boldsymbol{y}$ (i.e., the vector representing the radiation dose rates at all the pixels) conditioned on these three datasets ($\boldsymbol{z}_A$, $\boldsymbol{z}_C$ and $\boldsymbol{z}_W$), written as $p(\boldsymbol{y} \mid \boldsymbol{z}_A, \boldsymbol{z}_C, \boldsymbol{z}_W)$. By applying Bayes' rule, we can re-write this posterior distribution as:

(1) $p(\boldsymbol{y} \mid \boldsymbol{z}_A, \boldsymbol{z}_C, \boldsymbol{z}_W) \propto p(\boldsymbol{z}_A \mid \boldsymbol{y})\, p(\boldsymbol{z}_C \mid \boldsymbol{y})\, p(\boldsymbol{y} \mid \boldsymbol{z}_W)$

We assume that the datasets are conditionally independent of each other, given the air dose rate distribution $\boldsymbol{y}$.

Detailed descriptions of mathematical formulation are available in Wainwright et al. (2017). The first distributions $p(\boldsymbol{z}_A \mid \boldsymbol{y})$ and $p(\boldsymbol{z}_C \mid \boldsymbol{y})$ represent the data models to describe the low-resolution data (i.e., airborne and car survey data) as a function of the air dose rate map $\boldsymbol{y}$. The spatial average functions are included in these conditional distributions. For spatial averaging, Wainwright et al. (2017) have compared different averaging schemes based on the observation in the datasets. Based on their results, we use simple averaging for car survey data within the 100-m radius. We use weighted averaging to represent the large footprint of airborne survey, the weight of which is computed by the radiation transport simulations (Malins et al., 2016). The third distribution $p(\boldsymbol{y} \mid \boldsymbol{z}_W)$ represents the process model (i.e., geostatistical model) to describe the spatial pattern given the measured dose rates in the walk surveys. We also assume that the parameters in the data and process models are estimated and well-constrained through the exploratory data analysis and hence they are fixed during this Bayesian estimation. The correlation parameters are determined for each land-use class. After all the sub-models are defined and parameterized, the air dose rate map can be computed according to Eq. (1). We have defined different parameters in the data and process models for different land-cover types (Tables S1 and S2).

To characterize the temporal changes and their spatial variability, we define the dose rate reduction by the log-difference of the air dose rates in each year in a similar manner as Kinase et al. (2015). In this study, we first apply this integration method separately to the datasets in each year from 2014 to 2016 for creating three integrated maps at the 50-m resolution. The geostatistical and correlation parameters are determined separately for each year based on available datasets. This process provides snapshots of spatiotemporal dynamics of air dose rates in the region. We then analyze the spatial heterogeneity of the dose rate reduction to see whether it has been affected by decontamination or whether it is dependent on the land-use type.

We then temporally extrapolate the air dose rates by coupling this integrated map in 2016 with the data-driven ecological decay model developed by Kinase et al., 2014, Kinase et al., 2017. Since we assume the 2016 map as the initial condition, we can predict the air dose rate at time t_2 based on the known dose rate map at time t_1 ($t_1 = 2016$). We modify the equation in Kinase et al. (2014) as:

(2)D(t2)−DBGD(t1)−DBG={ffast0.5t2/Tfast+(1−ffast)0.5t2/Tslow}
{ffast0.5t1/Tfast+(1−ffast)0.5t1/
Tslow}ke−λ134t2+e−λ137t2ke−λ134t1+e−λ137t1

where $D(t)$ is the air dose rate at time t, D_{BG} is the background dose rate [μSv/h], f_{fast} is the fractional distribution of fast elimination component, T_{fast} is the ecological half-life for the fast elimination component, T_{slow} is the ecological half-life for the slow elimination component, $k$is the ambient dose equivalent rate ratio of ^{134}Cs and^{137}Cs at time zero, λ_{134} is the physical decay constant of ^{134}Cs, and λ_{137} is the physical decay constant of ^{137}Cs. In addition to the mean integrated map of radiation dose rates in 2016, we use the decay parameters determined through fitting in Kinase et al. (2017) or the same assumed parameters (Table S3) to create a predicted air dose rate map in 2026.

3. Results and discussions

The 2016 data on air dose rates are shown as an example in Fig. 2, which are the latest datasets currently available. Although the airborne survey (Fig. 2a) has the complete coverage of this region, the discrepancies are apparent between the airborne data and other ground-based measurements. In

particular, the airborne data show higher air dose rates compared to the car and walk survey data in the same regions. On the other hand, the car survey data are limited along the major roads (Fig. 2b), while the walk survey data are clustered in multiple small areas (Fig. 2c). The ground-based surveys alone cannot capture the spatial heterogeneity of the air dose rate distribution in the regional scale.

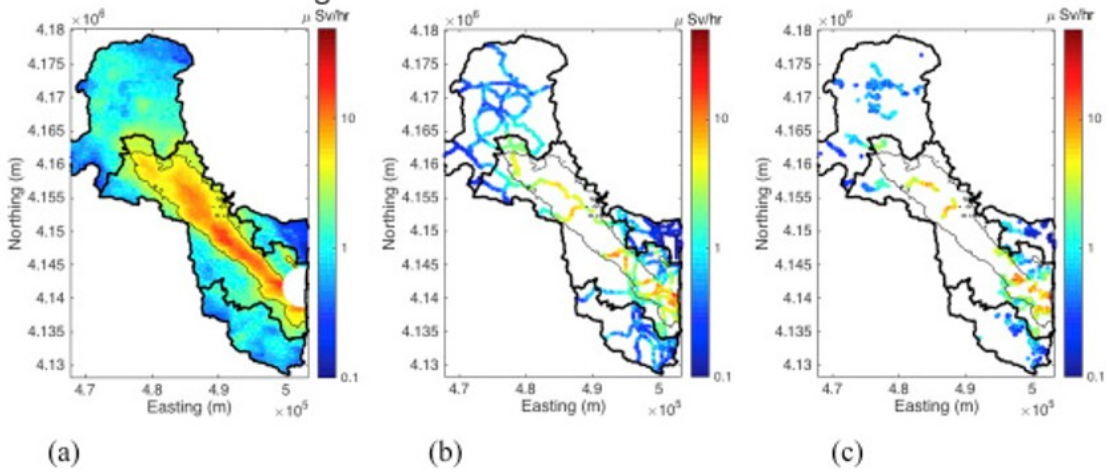

Fig. 2. Comparison among different types of datasets in 2016: (a) airborne survey, (b) car survey and (c) walk survey data. The thin black contour lines are the threshold of 3.8 μSv/h. The thick black lines are different zones within the evacuation designated area shown in Fig. 1a.

The comparison among different types of datasets (Fig. 3, Fig. 4) shows the discrepancy of air dose rates among them. Fig. 3 shows that the car and walk survey datasets are along the one-to-one lines, and highly correlated (the correlation coefficients of 0.96–0.97), when co-located data points are selected. Simple spatial averaging of walk survey data around each car data point improves the correlation coefficients to 0.99. The comparison between the airborne and walk survey datasets (Fig. 4) shows that the airborne survey data values are higher than the walk survey data even at the same locations, although the two types of data are significantly correlated (the correlation coefficients of 0.93–0.96). Weighted spatial averaging of the walk survey data around each airborne data point improves the correlation significantly to the correlation coefficients of 0.96–0.99. Several studies have found that the airborne survey data are consistently higher than co-located ground-based measurements (Naito et al., 2014; NRA, 2014; Yamashita and Itabashi, 2015; Miyazaki and Hayano, 2016; Wainwright et al., 2017; Kinase et al., 2017). To account such systematic shift in Fig. 4, a linear model was fitted with two parameters (i.e., slope and intercept) shown in Tables S1 and

S2. In Fig. 3, Fig. 4, the correlation coefficients are generally higher than the data from Fukushima City presented in Wainwright et al. (2017). This is due to the fact that the dose rates are higher in the evacuation zone than Fukushima City, as discussed in Wainwright et al. (2017).

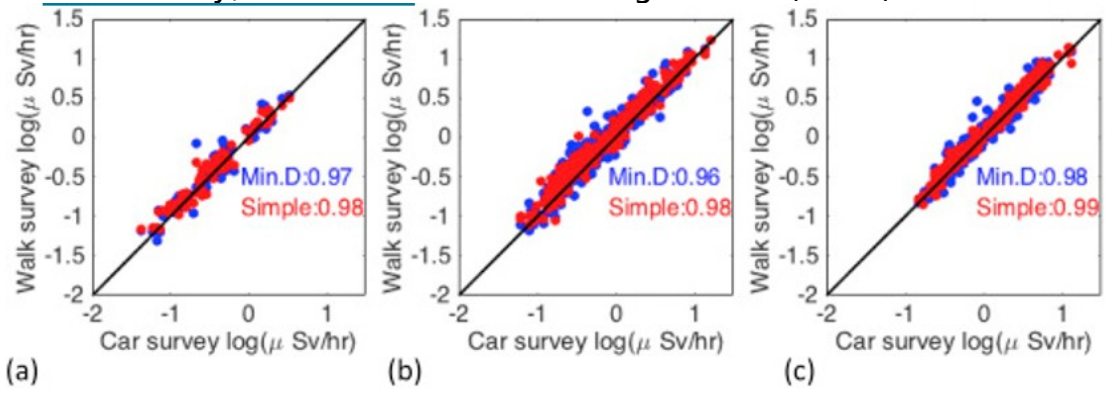

Fig. 3. Comparison between the car and walk survey data: (a) urban, (b) cropland, and (c) forest areas in the 2016 data. The blue circles ("Min. D") are the co-located points identified by the minimum distance. The red circles ("Simple") are the average of the walk survey points using the simple average. In each plot, the correlation coefficients are shown.

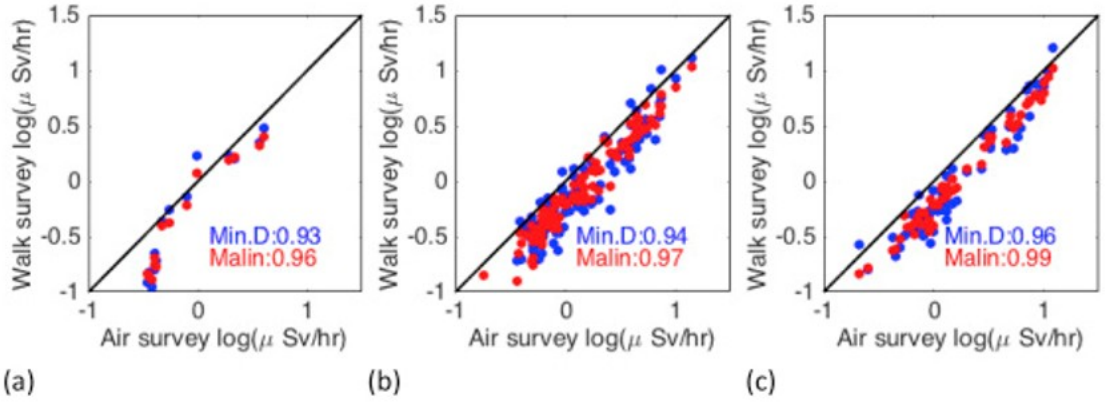

Fig. 4. Comparison between the air and walk survey data in: (a) urban, (b) cropland, and (c) forest and areas in the 2016 data. The blue circles ("Min. D") are the co-located points identified by the minimum distance. The red circles ("Malin") are the weighted average of the walk survey points using the weights computed by the radiation transport simulation. In each plot, the correlation coefficients are shown.

The three kinds of data were integrated using the developed method (Wainwright et al., 2017). A series of integrated maps from 2014 to 2016 (50 m by 50 m resolution) are compared to the airborne survey datasets in Fig. 5 (The zoom-up figures are available in Fig. S1). Both airborne data and integrated maps show that air dose rates are decreasing consistently across the region over the two years, and that the region above 3.8 μSv/h is shrinking. In general, the integrated maps (Fig. 5c–d) show more detailed

and finer-resolution heterogeneity than the original airborne data (Fig. 5a–c), although the general trend is very similar. The systematic bias (or shift) in the airborne data (Fig. 5a–c) is corrected in the integrated maps (Fig. 5d–f). For example, the area of above 3.8 μSv/h is 72.8 km^2 in the integrated map in 2016, which is significantly smaller than the one in the original airborne survey (141.3 km^2). The overestimation is quite significant so that the region above 3.8 μSv/h is larger in the airborne survey data in 2016 (Fig. 5c) than the 2015 integrated map (Fig. 5e). Correcting such overestimation would be important, since 3.8 μSv/h is considered to roughly correspond to an annual exposure dose of 20 mSv and often used as the threshold value for policy decision making.

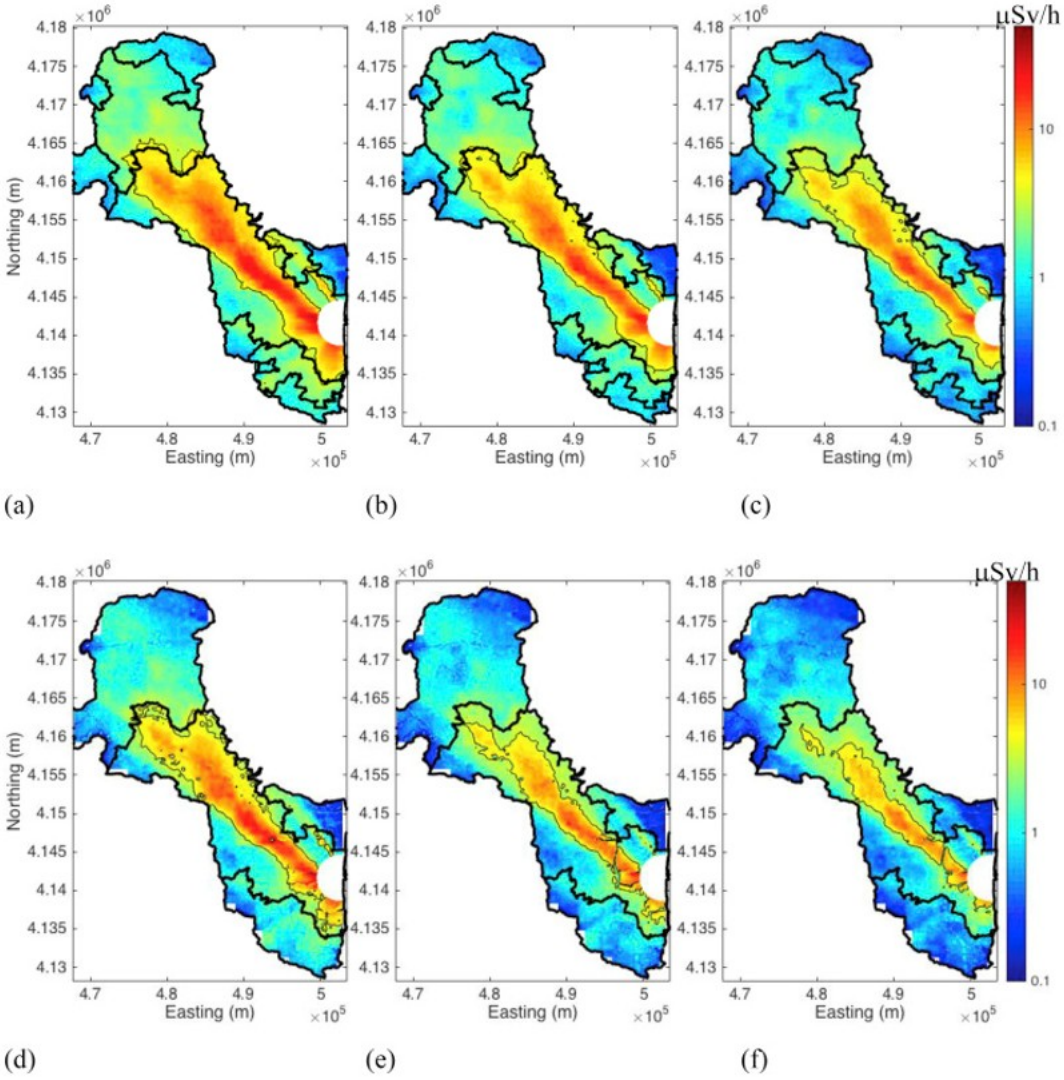

Fig. 5. Temporal evolution of (a–c) airborne survey data and (d–f) integrated maps in (a, d) 2014, (b, e) 2015 and (c, f) 2016. The thin black contour lines are the threshold of 3.8 μSv/h. The thick black lines are different zones within the evacuation designated area shown in Fig. 1a.

The performance of the integrated maps was confirmed by the validation (Fig. 6), using one hundred points of the walk survey data excluded from the estimation. Without the data integration, the airborne data at co-located points (blue dots) exhibit larger scatters and a systematic bias compared to the co-located walk survey data. After the data integration, the predicted values (based on our approach and the three datasets) are tightly distributed around the one-to-one line and are mostly included in the 99% confidence interval. The validation result (Fig. 6) shows that this method successfully estimates the fine-resolution dose-rate map based on the spatially sparse walk and car survey data and airborne data.

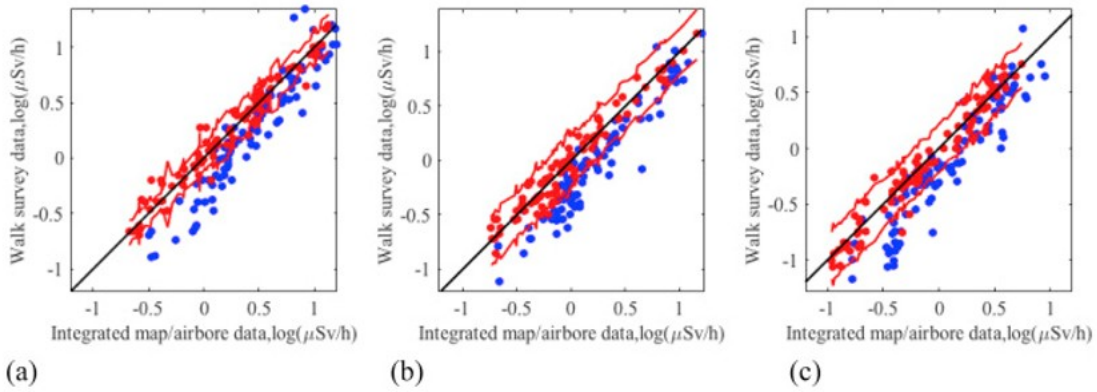

Fig. 6. Validation results: comparison of the log-transformed walk survey data to the integrated map (red circles) and to the co-located airborne data (blue circles) at the walk-survey data locations not used for the estimation in (a) 2014, (b) 2015 and (c) 2016. The red dots represent the predicted values based on the data integration method; the blue dots are the co-located airborne data without using the integration. The black line is the one-to-one line; the red lines are the 99% confidence intervals.

Fig. 7 shows the log-difference in the air dose rates between two consecutive years calculated from the integrated maps shown in Fig. 5. Although the east-west lines associated with the flight lines can be seen as an artifact in the forested region, we can still see significant anthropologic effects. The artifact is relatively small (5–10% of the dose rates) so that it is noticeable only in this reduction map (Fig. 7): not in the integrated map or airborne data (Fig. 5). The artifact was corrected within the urban or cropland areas where the walk and car survey datasets are available. Between 2014 and 2015, the Joban highway was opened with a fresh pavement without contamination, which shows as a large reduction along the north-south road in the

southwest part of the domain (Fig. 7a). The decontamination activity was known to be particularly active in the southwest region of the domain (Tomioka Village). Between 2015 and 2016, the decontamination was active in the northwestern region (Minami-soma City), which can be seen in Fig. 7b. This is the first time that the decontamination effect is visualized in the regional scale. After the Chernobyl accident, regional-scale decontamination was found to be ineffective due to re-contamination (Vovk et al., 1993). After the Fukushima accident, extensive research and investigation have been made in decontamination technologies and applications (Miyahara et al., 2012). Our results show that the decontamination is quite effective to reduce the air dose rates.

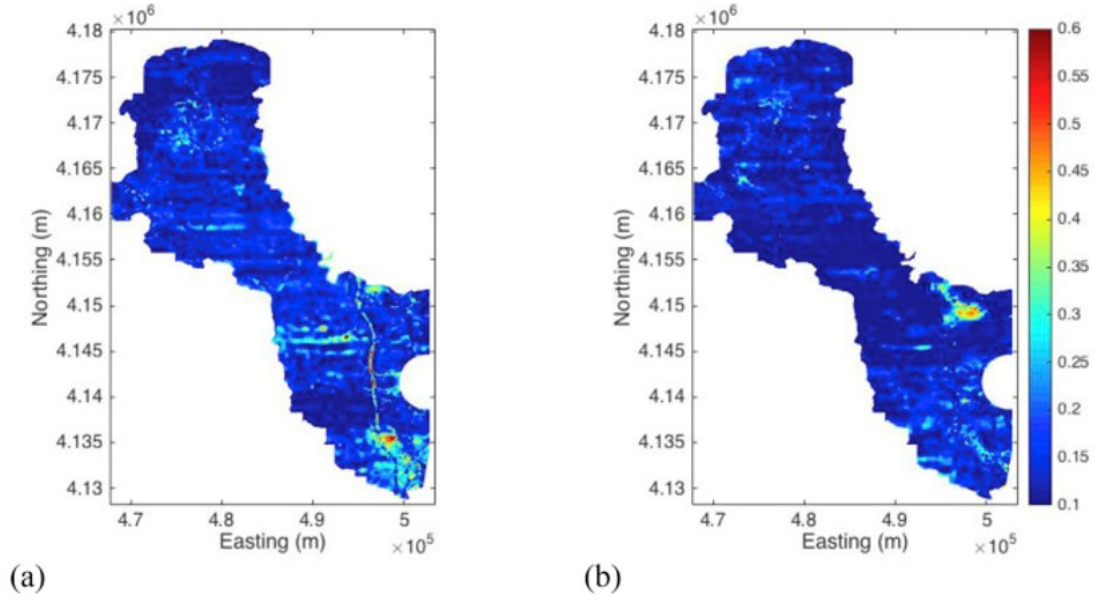

Fig. 7. Log-difference of the air dose rates between (a) 2014–2015 and (b) 2015–2016.

The dose rate reduction of air dose rates was computed at each pixel, and summarized in each land-use class as the median and five and ninety-five percentiles (Table 1). The urban area has a large reduction as well as a large variability in the reduction, which suggests the effect of paved surfaces on the mobility of radiocesium (e.g. roads) as well as anthropologic effects (e.g., decontamination and traffic) consistent with previous studies (e.g., Kinase et al., 2014; Kinase et al., 2017; Saito, 2016). The reduction is larger than the computed median values in each land-use type based on the data-driven model in Kinase et al. (2017). This suggests that the regional-scale ecological half-life for the fast and slow elimination components could be smaller or the fast elimination fraction could be larger than the values used in Kinase et al.

(2017). In addition, the reduction is smaller in 2015–2016 than 2014–2015, suggesting the decreasing fraction of ^{134}Cs. We expect the reduction rate would decrease in the future, although the reduction would remain larger than the physical decay due to the radiocesium transport in the environment.

Table 1. Median reduction in the air dose rate within each land-use type, along with the range of the five and ninety-five percentiles in the prentices. The reduction was defined by the ratio of air dose rates between the 2 years at each pixel.

	2014–2015	2015–2016	2014–2016
Urban	0.68 (0.46–0.95)	0.74 (0.40–1.00)	0.50 (0.25–0.75)
Cropland	0.70 (0.46–0.89)	0.72 (0.47–0.93)	0.50 (0.28–0.71)
Forest	0.72 (0.57–0.86)	0.78 (0.63–0.95)	0.57 (0.42–0.70)
Kinase model(forest)[a]	0.83 (0.79–0.87)	0.86 (0.82–0.89)	0.72 (0.65–0.77)
Kinase model (others)[a]	0.83 (0.78–0.87)	0.86 (0.81–0.89)	0.72 (0.64–0.77)

a

Kinase et al. (2017).

Fig. 8 shows the predicted maps in 2026 based on the 2016 integrated map (the enlarged version is available in the supporting information as Fig. S2). The prediction is based on the assumptions that the ecological decay continues at the current rate, and that the decontamination is not considered. The air dose rates continue to decrease, and the region above 3.8 μSv/h is predicted to shrink significantly in 2026. Since we used the parameters from Kinase et al. (2017), the actual reduction could be faster than this map. Although there is still a remaining area above 3.8 μSv/h, this area is almost fully contained within the non-residential forested zone. The area above 3.8 μSv/h is 14.2 km^2, 97.8% of which is in the forested area.

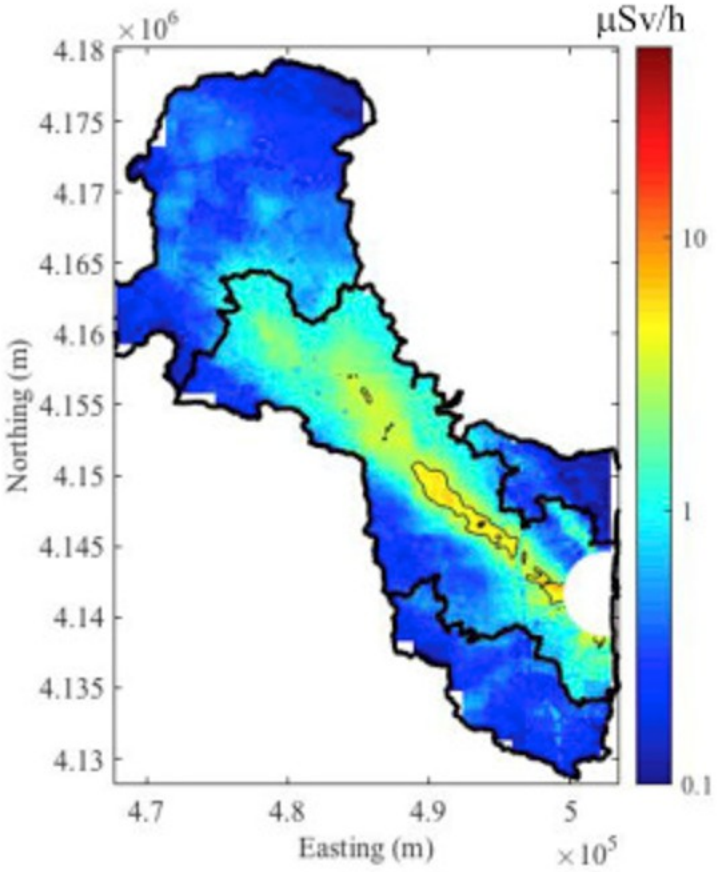

Fig. 8. Predicted air dose rate in 2026 based on the integrated map. The thin black contour lines are the threshold of 3.8 μSv/h. The thick black lines are different zones within the evacuation designated area.

The effectiveness of remediation in the forested region has been debated since the accident, since the soil, plant and/or litter removal leads to significant ecological disturbance (Ayabe et al., 2017). Globally, there has been a paradigm shift in environmental remediation from an approach of

intense soil removal and treatment to one of passive remediation or natural attenuation (Ellis and Hadley, 2009). Such sustainable remediation considers *net environmental impacts* including ecological disturbances, waste generation and energy usage. Also, it promotes longer institutional control with alternative end-use of the restricted land. Our prediction – that contamination will be limited within the non-residential forested zone in 10 years – could have an impact on decontamination planning in the sustainable remediation framework. For example, focusing decontamination in the residential areas would be more effective for the residents' return while avoiding ecological disturbances in forested regions and reducing cost and waste.

4. Conclusion

In this study, we characterized the regional-scale changes in the air dose rates within the evacuation designated area around the Fukushima Dai-ichi Nuclear Power Plant. We first applied the Bayesian data integration approach to create the integrated maps of air dose rates in 2014, 2015 and 2016, based on multi-type multiscale datasets available in the region. We quantified the ecological half-life and dose-rate reduction depending on land-use types, and then coupled the integrated map with the data-driven predictive model to predict the future radiation air dose rates with increased accuracy.

This was the second demonstration of our Bayesian data-integration approach developed by Wainwright et al. (2017) in a higher-dose region and in the larger spatial scale. The results have again shown that the proposed method was effective to integrate multiscale, multi-type dose-rate measurements, and also to create the high-resolution air dose rates over the large spatial extent. The validation has confirmed a consistent performance of this method over these three years. Integrated maps captured more detailed spatial heterogeneity than the regional airborne survey data, and corrected a significant positive bias in the airborne survey.

The integrated maps enable us to visualize the temporal changes of air-dose rates in the regional scale. The dose rate reduction was computed based on these integrated maps, and the reduction was shown to be smaller in the forested region than the other land-use types, which is consistent with previous studies (Kinase et al., 2014; Saito, 2016). The integrated maps were

particularly powerful in identifying anthropologic effects such as the re-opening of roads and effects of decontamination. In addition, the predictive modeling results showed that by 2026, the air dose rates would continue to decrease, and the area above 3.8 μSv/h would be almost fully contained within the non-residential forested zone.

Acknowledgement

The environmental monitoring data in this study were acquired during the projects commissioned by the Japan Nuclear Regulatory Agency. We thank the people who contributed to collecting the data and compiling them into the JAEA database. Funding for this work was provided by Japan Atomic Energy Agency under Award No. AWD00000626, as part of Work for Others funding from Berkeley Lab, provided by the U.S. Department of Energy under Contract No. DE-AC02-05CH11231.

References

Andoh et al., 2015
M. Andoh, Y. Nakahara, S. Tsuda, T. Yoshida, N. Matsuda, F. Takahashi, K. Takamiya**Measurement of air dose rates over a wide area around the Fukushima Dai-ichi Nuclear Power Plant through a series of car-borne surveys**
J. Environ. Radioact., 139 (2015), pp. 266-280
Ayabe et al., 2017
Y. Ayabe, N. Hijii, C. Takenaka**Effects of local-scale decontamination in a secondary forest contaminated after the Fukushima nuclear power plant accident**
Environ. Pollut., 228 (2017), pp. 344-353
Deutsch and Journel, 1998
C.V. Deutsch, A.G. Journel**GSLIB: Geostatistical Software Library and User's Guide.**
Oxford Univ. Press, New York (1998)
GSLIB: Geostatistical Software Library and User's Guide. 2nd ed. Oxford Univ. Press, New York
Ribeiro and Diggle, 2007
P.J. Ribeiro Jr., P.J. Diggle**Model Based Geostatistics**
Springer Series in Statistics (2007)
Ellis and Hadley, 2009

D.E. Ellis, P.W. Hadley**Sustainable remediation white paper - integrating sustainable principles, practices, and metrics into remediation projects**
Remed. J., 19 (3) (2009)
5–114
https://doi.org/10.1002/rem.20210
Fukushima Prefectural Government, 2017
Fukushima Prefectural Government, http://www.pref.fukushima.lg.jp/site/portal-english/en03-08.html, retrieved on December 19th, 2017.
Kinase et al., 2014
S. Kinase, T. Takahashi, S. Sato, R. Sakamoto, K. Saito**Development of prediction models for radioactive caesium distribution within the 80-km radius of the Fukushima Daiichi nuclear power plant**
Radiat. Protect. Dosim., 160 (4) (2014), pp. 318-321
Kinase et al., 2015
S. Kinase, S. Sato, R. Sakamoto, H. Yamamoto, K. Saito**Changes in ambient dose equivalent rates around roads at Kawamata town after the Fukushima accident**
Radiat. Protect. Dosim., 167 (1–3) (2015), pp. 340-343
Kinase et al., 2017
S. Kinase, T. Takahashi, K. Saito**Long-term predictions of ambient dose equivalent rates after the Fukushima Daiichi nuclear power plant accident**
J. Nucl. Sci. Technol. (2017), pp. 1-10
Kitamura et al., 2014
A. Kitamura, M. Yamaguchi, H. Kurikami, M. Yui, Y. Onishi**Predicting sediment and cesium-137 discharge from catchments in eastern Fukushima**
Anthropocene, 5 (2014), pp. 22-31
Malins et al., 2016
A. Malins, H. Kurikami, S. Nakama, T. Saito, M. Okumura, M. Machida, A. Kita mura**Evaluation of ambient dose equivalent rates influenced by vertical and horizontal distribution of radiocesium in soil in Fukushima Prefecture**
J. Environ. Radioact., 151 (2016), pp. 38-49
Mikami et al., 2015a
S. Mikami, T. Maeyama, Y. Hoshide, R. Sakamoto, S. Sato, N. Okuda, K. Saito **The air dose rate around the Fukushima Dai-ichi Nuclear Power**

Plant: its spatial characteristics and temporal changes until December 2012
J. Environ. Radioact., 139 (2015), pp. 250-259
Mikami et al., 2015b
S. Mikami, T. Maeyama, Y. Hoshide, R. Sakamoto, S. Sato, N. Okuda, M. Fujiwara**Spatial distributions of radionuclides deposited onto ground soil around the Fukushima Dai-ichi Nuclear Power Plant and their temporal change until December 2012**
J. Environ. Radioact., 139 (2015), pp. 320-343
Miyahara et al., 2012
K. Miyahara, T. Tokizawa, S. Nakayama**Overview of the Results of Fukushima Decontamination Pilot Projects**
Japan Atomic Energy Agency (2012)
Miyazaki and Hayano, 2016
M. Miyazaki, R. Hayano**Individual external dose monitoring of all citizens of Date City by passive dosimeter 5 to 51 months after the Fukushima NPP accident (series): 1. Comparison of individual dose with ambient dose rate monitored by aircraft surveys**
J. Radiol. Prot., 37 (1) (2016), p. 1
Naito et al., 2014
W. Naito, M. Uesaka, C. Yamada, H. Ishii**Evaluation of dose from external irradiation for individuals living in areas affected by the Fukushima Daiichi Nuclear Plant accident**
Radiat. Protect. Dosim., 163 (3) (2014), pp. 353-361
NRA, 2014
Nuclear Regulation Authority**Characterizing the long-term effects of radionuclide deposition after the Fukushima dai-ichi nuclear power plant accident, Japanese**
Available from:
http://radioactivity.nsr.go.jp/ja/list/504/list-1.html (2014)
Peles et al., 2002
J.D. Peles, M.H. Smith, I.L. Brisbin**Ecological half-life of 137 Cs in plants associated with a contaminated stream**
J. Environ. Radioact., 59 (2) (2002), pp. 169-178
Saito, 2016
K. Saito**Features of exposure doses to the public due to the Fukushima accident**
Global Environ. Res., 20 (2016), pp. 67-72
Saito and Onda, 2015

K. Saito, Y. Onda**Outline of the National Mapping Projects Implemented after the Fukushima Accident**
(2015)
Saito et al., 2015
K. Saito, I. Tanihata, M. Fujiwara, T. Saito, S. Shimoura, T. Otsuka, N. Kinouchi **Detailed deposition density maps constructed by large-scale soil sampling for gamma-ray emitting radioactive nuclides from the Fukushima Dai-ichi Nuclear Power Plant accident**
J. Environ. Radioact., 139 (2015), pp. 308-319
Seki et al., 2014
A. Seki, O. Saito, H. Nago, K. Suzuki, K. Tomishima, K. Saito, H. Takemiya**Dev elopment of a software platform for providing environmental monitoring data for the Fukushima Daiichi nuclear accident**
Radiat. Protect. Dosim., 164 (1–2) (2014), pp. 97-102
Takahashi et al., 2013
M. Takahashi, K.N. Nasahara, T. Tadono, T. Watanabe, M. Dotsu, T. Sugimura, N.Tomiyama**JAXA high resolution land-use and land-cover map of Japan**
Geoscience and Remote Sensing Symposium (IGARSS), 2013 IEEE International, IEEE (2013, July), pp. 2384-2387
Tanaka, 2012
S. Tanaka**Accident at the Fukushima dai-ichi nuclear power stations of TEPCO —outline & lessons learned**
Proc. Jpn. Acad. Ser. B Phys. Biol. Sci., 88 (9) (2012), pp. 471-484
Tanigaki et al., 2013
M. Tanigaki, R. Okumura, K. Takamiya, N. Sato, H. Yoshino, H. Yamana**Devel opment of a car-borne γ-ray survey system, KURAMA**
Nucl. Instrum. Methods Phys. Res. Sect. A Accel. Spectrom. Detect. Assoc. Equip., 726 (2013), pp. 162-168
Torii et al., 2012
T. Torii, Y. Sanada, T. Sugita, A. Kondo, Y. Shikaze, Y. Urabe**Investigation of Radionuclide Distribution Using Aircraft for Surrounding Environmental Survey From Fukushima Daiichi Nuclear Power Plant, JAEA-Technology 2012-036**
(Dec 2012)
192 p. (in Japanese)
http://dx.doi.org/10.11484/JAEA-Technology-2012-036
Tsuda et al., 2015

S. Tsuda, T. Yoshida, M. Tsutsumi, K. Saito**Characteristics and verification of a car-borne survey system for dose rates in air: KURAMA-II**
J. Environ. Radioact., 139 (2015), pp. 260-265
Vovk et al., 1993
I.F. Vovk, V.V. Blagoyev, A.N. Lyashenko, I.S. Kovalev**Technical approaches to decontamination of terrestrial environments in the CIS (former USSR)**
Sci. Total Environ., 137 (1–3) (1993), pp. 49-63
Wainwright et al., 2017
H.M. Wainwright, A. Seki, J. Chen, K. Saito**A multiscale Bayesian data integration approach for mapping air dose rates around the Fukushima Daiichi Nuclear Power Plant**
J. Environ. Radioact., 167 (2017), pp. 62-69
Wei et al., 2017
L. Wei, T. Kinouchi, K. Yoshimura, M.L. Velleux**Modeling watershed-scale 137 Cs transport in a forested catchment affected by the Fukushima Dai-ichi Nuclear Power Plant accident**
J. Environ. Radioact., 171 (2017), pp. 21-33
Wikle et al., 2001
C.K. Wikle, R.F. Milliff, D. Nychka, L.M. Berliner**Spatiotemporal hierarchical Bayesian modeling: tropical ocean surface winds**
J. Am. Stat. Assoc., 96 (454) (2001), pp. 382-397
Yamashita and Itabashi, 2015
T. Yamashita, K. Itabashi**Technical support of decontamination projects and communication activity for residents to understand radiation. Activities for the environmental recovery by JAEA (3)**
Nippon Genshiryoku Gakkai Shi, 57 (10) (2015), pp. 656-661
Yasutaka et al., 2013
T. Yasutaka, Y. Iwasaki, S. Hashimoto, W. Naito, K. Ono, A. Kishimoto, J. Naka nishi**A GIS-based evaluation of the effect of decontamination on effective doses due to long-term external exposures in Fukushima**
Chemosphere, 93 (6) (2013), pp. 1222-1229